Available online at www.sciencedirect.com

ScienceDirect

Acta Materialia 92 (2015) 72–80

Acta MATERIALIA

www.elsevier.com/locate/actamat

Ab initio study of intrinsic point defects in PbTe: an insight into phase stability

Saurabh Bajaj,[a] Gregory S. Pomrehn,[a] Jeff W. Doak,[b] Wojciech Gierlotka,[c] Hsin-jay Wu,[d] Sinn-Wen Chen,[e] Chris Wolverton,[b] William A. Goddard, III[a] and G. Jeffrey Snyder[a,b,*]

[a]*Department of Applied Physics and Materials Science, California Institute of Technology, Pasadena, CA 91125, United States*
[b]*Department of Materials Science and Engineering, Northwestern University, Evanston, IL 60208, United States*
[c]*Department of Material Science and Engineering, National Dong Hwa University, Taiwan*
[d]*Department of Materials and Optoelectronic science, National Sun Yat-sen University, Kaohsiung 80424, Taiwan*
[e]*Department of Chemical Engineering, National Tsing Hua University, #101, Section 2, Kuang-Fu Rd., Hsin-Chu 300, Taiwan*

Received 20 November 2014; revised 23 January 2015; accepted 18 March 2015
Available online 13 April 2015

Abstract—The stability of intrinsic point defects in PbTe, one of the most widely studied and efficient thermoelectric material, is explored by means of Density Functional Theory (DFT). The origin of *n*- and *p*-type conductivity in PbTe is attributed to particular intrinsic charged defects by calculating their formation energies. These DFT calculated defect formation energies are then used in the Gibbs free energy description of this phase as part of the Pb-Te thermodynamic model built using the CALPHAD method, and in the resulting phase diagram it is found that its solubility lines and non-stoichiometric range agree very well with experimental data. Such an approach of using DFT in conjunction with CALPHAD for compound semiconductor phases that exhibit very small ranges of non-stoichiometry does not only make the process of calculating phase diagrams for such systems more physical, but is necessary and critical for the assessment of unknown phase diagrams.

Keywords: Point defects; Thermoelectric; DFT; CALPHAD

1. Introduction

One solution to the rapidly changing climate and global warming is to extract the available energy (or exergy) from waste heat, and convert it to electricity. Devices that perform such an operation are called thermoelectric generators, and materials used in these devices are known as thermoelectric (TE) materials. The lead chalcogenide salt PbTe, one of the most widely studied TE material, is a IV–VI semiconductor with a small band-gap and is the best performing TE material for mid-temperature power generation (200–600 °C) [1]. It exhibits both types of conductivity depending on the growth conditions- *n*-type (electrons) in a Pb-rich environment and *p*-type (holes) in a Te-rich environment [2–5,7,8,6], which makes it particularly advantageous since TE devices consist of both *n*- and *p*-type legs coupled together. Furthermore, tuning the carrier densities by adjusting the defect/dopant concentrations not only maximizes zT, but also gives control over where its peak occurs in the temperature space [1]. This coupling between carrier concentration, defects/dopants, and zT makes it important to understand the defect chemistry of a material for its application as a thermoelectric material.

In a previous study by Ahmad et al. [9], the physics and electronic structure of vacancy and impurity induced deep defect states in PbTe was investigated by *ab initio* calculations. Another study by Xiong et al. [10] investigated the impact of dopants on the density of states (DOS) and band structures between pure and extrinsically doped PbTe. Both these works have not investigated the energetics of different types of point defects in intrinsic PbTe. In a recent publication by Wang et al. [11], spin–orbit coupling (SOC) calculations were performed that result in a band gap of 0.11 eV which is in better agreement with the room temperature experimental band gap of 0.31 eV. However, it was found that the fermi level is positioned where Te vacancy V_{Te}^{+2} donor defects for Pb-rich and Te substitutional Te_{Pb}^{+2} donor defects for Te-rich conditions are most stable, thus leading to *n*-type conductivity for both growth conditions. *p*-type/hole conductivity for Te-rich conditions was found to only occur for a limited set of Te chemical potential. This result is inconsistent with the well-known observance of both electron and hole conductivity in PbTe from numerous experimental works. Additionally, no comparison with experimental results on

* Corresponding author at: Department of Materials Science and Engineering, Northwestern University, Evanston, IL 60208, United States. Tel.: +1 626 395 6220; e-mail: jeff.snyder@northwestern.edu

http://dx.doi.org/10.1016/j.actamat.2015.03.034
1359-6462/

carrier concentrations is made. Thus, in this work, we investigate the role of intrinsic point defects in the conductivity and doping behavior of PbTe within the framework of Density Functional Theory (DFT). Specifically, we study the stability of vacancy, anti-site, and interstitial defects by calculating their formation energies for both Pb-rich and Te-rich growth conditions. Defects with the lowest formation energies will help us attribute the origins of *n*-type and *p*-type conductivity in PbTe to that specific type of point defect type.

The phase diagram of Pb-Te exhibits a very small range of non-stoichiometry in the PbTe phase to the order of $x = 10^{-4}$ on both sides of the stoichiometric line at $x = 0.50$ [2–5,7,8,6] due to the presence of defects, that in turn leads to the *n*- and *p*-type conductivity in this phase. A previously developed thermodynamic model of this system by Gierlotka et al. [12] describes the Gibbs energy of this compound using the Wagner–Schottky defect model [13] that assumes anti-site defects - $(Pb, Te)_1$: $(Te, Pb)_1$ to cause the very small non-homogeneity range. However, as we shall see later, it is actually the vacancy defects that have the lowest formation energy and hence are the most stable among different types of defects. Thus, in this work, we use the CALculation of PHAse Diagrams (CALPHAD) method [14] to modify the description of the PbTe phase, and then use the DFT vacancy formation energy values in its Gibbs free energy expressions which result in solubility lines that agree very well with experimental data. This approach of using information from DFT to select a particular type of phase model and use the DFT calculated defect formation energies in the Gibbs free energy descriptions to calculate a phase diagram makes the process of building thermodynamic models more physical. More importantly, in the field of TE materials where dopants are added in small concentrations to fine tune TE properties, this methodology helps determine the solubility ranges of those dopants in the base material.

2. Methodology

2.1. Defect thermodynamics

The stability of a defect is determined by its formation energy, which according to the Zhang–Northrup supercell formalism [15] for a defect D of charge q is given by

$$\Delta H_{d,q} = [E_{d,q} - E_H] + \sum_{\alpha} n_\alpha(\mu_\alpha^0 + \Delta\mu_\alpha) + q(E_{VBM} + \Delta V_{PA} + \mu_e) + \Delta E_{IC}, \quad (1)$$

where, $E_{d,q}$ and E_H are the total energies of the defect containing supercell and the ideal supercell, respectively, and represent the bond energy cost due to the creation of a defect. The atomic chemical potentials μ_α is the energy of the atomic reservoir of the atoms either removed ($n_\alpha = +1$) or added ($n_\alpha = -1$) to the host supercell in the formation of a defect. It reflects the crystal growth conditions as $\mu_\alpha = \mu_\alpha^0 + \Delta\mu_\alpha$ where μ_α^0 is the chemical potential of an element in its standard reference state (the phase in equilibrium at conditions of room temperature and pressure, T = 298 K and P = 1 atm), and $\Delta\mu_\alpha$ is the change in chemical potential of an element with reference to its standard state. For a maximally rich growth environment of an element, $\Delta\mu_\alpha = 0$. For example, Pb-rich/Te-poor growth environment in PbTe is represented by $\mu_{Pb} = \mu_{Pb}^0$ ($\Delta\mu_{Pb} = 0$). In these conditions, the chemical potential of Te is reduced to below the value for its standard reference state value, i.e. $\mu_{Te} < \mu_{Te}^0 (\Delta\mu_{Te} < 0)$. Its exact value is given by the condition that correlates the elemental chemical potential for the stability of this phase,

$$\mu_{Pb} + \mu_{Te} = \mu_{PbTe}, \quad (2)$$

where, μ_{PbTe} is the chemical potential of the defect-free PbTe compound. The above condition is true in the case of PbTe since there are no other competing phases in the phase stability regions between the elemental reference phases and the PbTe phase.

For charged defects ($q \neq 0$), the second to last term in Eq. (1), i.e. $q(E_{VBM} + \Delta V_{PA} + \mu_e)$, represents the energy cost of exchanging electrons with the electron reservoir. E_{VBM}, the valence band maximum (VBM) energy corresponds to the energy of the highest occupied level. It is the cost of removing an electron from the top of the valence band, and in this work the energy difference between a neutral defect-free supercell and the supercell with a hole is used to approximate the value of E_{VBM}.

The creation of a neutral defect in a supercell causes the band energy levels to shift relative to the levels in the defect-free supercell. Furthermore, in the case of creation of a charged defect, the charge neutrality condition is violated which causes the Coulomb potential to diverge. This is avoided by setting $V_{el}(G = 0) = 0$ that is equivalent to introducing a compensating uniform background charge which only affects the potential, and not the charge density in the calculation. Thus, the energy levels of the charged defect cell do not reference to the potential of the host cell, and the defect energy levels need to be re-aligned to the host energy levels using a potential alignment (PA) term ΔV_{PA} that is added to the defect formation energy (in Eq. (1) above) and is calculated as [16],

$$\Delta E_{PA} = q.\Delta V_{PA} = q.(V_{d,q}^r - V_H^r), \quad (3)$$

where, ΔV_{PA} is the potential alignment between the spherically-averaged electrostatic potentials of the defect ($V_{d,q}^r$) and the host (V_H^r) cells far from the defect site so as to avoid including any spurious chemical interactions with the defect. In this work, it is found that ΔE_{PA} ranges from 0.25 eV to 0.05 eV for the various defects. Finally, the electron chemical potential μ_e term in Eq. (1) is the additional energy of electrons in our system, and is set to range between the VBM and CBM (conduction band minimum) for plots showing the variation of defect formation energies as functions of electron chemical potential. Its value is fixed as a function of temperature by solving the charge neutrality condition, as explained later in Section 3.1.

The use of periodic boundary conditions in DFT causes charged defects to be periodically and infinitely repeated in neighboring supercells. These periodic images of defects result in electrostatic interactions between the charges, and defect concentrations in the order of tenths of a percent which is significantly higher than that found in semiconductors (parts-per-million). Also, the computing demands posed by DFT limit the size of supercells that can be used to perform calculations on. Thus, in order to model a true isolated charge defect in a size limited supercell in non-degenerate conditions, an image charge correction energy term ΔE_{IC} is added to the defect formation energy in Eq. (1) above. It is typically written in the form of a multipole expansion given by Makov and Payne [17],

$$\Delta E_{IC} = \frac{q^2\alpha}{2\epsilon L} + \frac{2\pi q Q_r}{3\epsilon L^3} + O(L^{-5}). \quad (4)$$

The first two terms are the monopole and quadrupole corrections where α is the Madelung constant of the supercell lattice (1.75 for the rock salt NaCl structure of PbTe), L is distance between defects, ϵ is the static dielectric constant which is calculated to be equal to 397 (including ionic contributions) for PbTe using density functional perturbation theory as implemented in VASP [18–20], and is in good agreement with available experimental data (412 ± 40) [21]. Q_r is the second radial moment of the charge density, and it has been found [16] that the quadrupole term is typically $\approx -35\%$ of the monopole term which is implemented here. It is also found from Ref. [16] that these terms are not affected by the choice of the exchange-correlation functional. Higher order terms $O(L^{-5})$ are neglected due to their minimal contributions. All together, the image charge correction term is calculated to have a maximum value of $\approx$0.01 eV in this work for $q \pm 2$ charges.

2.2. Computational details

DFT calculations are performed with the Vienna Ab-initio Simulation Package (VASP) [22–25] using the Projector Augmented Wave (PAW) method [26–28] and generalized gradient approximation (GGA) with the exchange–correlation functional of Perdew, Burke, and Ernzerhof (PBE) [29]. The $5d^{10}6s^26p^2$ orbitals of Pb and $5s^25p^4$ orbitals of Te were treated as valence states to generate the PAW potentials. The primitive cell of PbTe contains 2 atoms, and all calculations are performed on a $5 \times 5 \times 5$ supercell of the primitive cell that contains 250 atoms. The cutoff energy of plane wave basis was set to 400 eV, and integrations over the first Brillouin zone were made using a k-point grid set of $2 \times 2 \times 2$ generated according to the Monkhorst–Pack scheme [30]. Unit cell parameters and atomic positions were relaxed based on an energy convergence criteria of 10^{-4} eV, and a final static calculation was performed for an accurate total energy.

2.3. Thermodynamic models for the CALPHAD method

The thermodynamic models employed in this work are based on previous assessments by Gierlotka et al. [12,31] on the Pb-Te system. In these expressions, the Gibbs energies G_m^{ϕ} of each phase ϕ taking part in the equilibria are defined using the models described below. x_i is the molar fraction of component i, and ${}^oG_i^{\phi}$ is the reference Gibbs energy of the component i making up the phase at 298 K and 1 atm that is obtained from the Scientific Group Thermodata Europe (SGTE) database [32].

2.3.1. Liquid

The liquid phase of the Pb-Te system exhibits a sharp minimum versus composition in its enthalpy of mixing near the PbTe stoichiometry that indicates strong short-range order interactions [33], which has also been seen in experimental measurements on its conductivity [34] and viscosity [35]. Thus, following Ref. [31], in this work we have also used the associate model [36] to describe this phase. In CALPHAD terminology, the term "associate" is used to denote an association between unlike atoms when the attractive forces between the atoms are not strong enough to form a stable chemical molecule. According to this model, the Gibbs energy per mole of atoms of such a phase is given by,

$$G_m^{Liq} = G_{ref} + \Delta G_{mix}^{ideal} + \Delta G_{mix}^{xs} = \frac{\left[\sum_i x_i^o G_i^{Liq} + RT\sum_i x_i \ln x_i + \sum_i \sum_{j>1} x_i x_j \sum_v {}^vL_{i,j}^{Liq}(x_i - x_j)^v\right]}{(1 + x_{PbTe})}, \quad (5)$$

where, $i, j =$ Pb, Te, and PbTe, R is the gas constant, and T is the temperature. ${}^vL_{i,j}^{Liq}$ is called the non-ideal interaction parameter, and is part of the excess Gibbs energy of mixing term ΔG_{mix}^{xs} which includes temperature dependency of sources of entropy (non-ideal configurational, vibrational, and electronic) apart from the ideal configurational entropy ΔG_{mix}^{ideal}. The temperature dependency in these parameters is included by expanding them as,

$${}^vL_{i,j}^{Liq} = {}^vA_{i,j}^{Liq} + {}^vB_{i,j}^{Liq}.T, \quad (6)$$

where, ${}^vA_{i,j}^{Liq}$ and ${}^vB_{i,j}^{Liq}$, the only unknowns in Eq. (5) above, are user-defined parameters that are fitted in the CALPHAD method to experimental and/or *ab initio* data on phase equilibria/diagram and thermodynamic properties.

2.3.2. PbTe

The PbTe structure is of rock salt NaCl structure with space group $Fm\bar{3}m$ (No. 225). As mentioned earlier in the Introduction, the small non-stoichiometry in the PbTe phase that is caused by defects is modeled using the Wagner–Schottky sublattice model [13], but now using vacancies as defects, i.e. $(Pb, Va)_1$:$(Te, Va)_1$ instead of anti-site defects assumed before [12]. The Gibbs energy of this phase is given by,

$$G_m^{PbTe} = \sum_{I0} P_{I0}(y)\,{}^oG_{I0}^{\phi} + RT\sum_s N^s \sum_i {}^sy_i \ln {}^sy_i + \sum_{Z>0}\sum_{IZ} P_{IZ}(y) L_{IZ}^{\phi}, \quad (7)$$

where, P_{I0} is a product of sublattice site fractions when each of them is occupied by only one component, N^s is the number of sites on sublattice s, P_{IZ} is also a product of sublattice site fractions but when only one sublattice contains Z components and the remaining are occupied by one component, and ${}^sy_i$ is called the site fraction defined by:

$${}^sy_i = \frac{n_i^s}{N^s}, \quad (8)$$

where n_i^s is the number of atoms of component i on sublattice s. For the vacancy model of the PbTe phase, this simplifies to,

$$G_m^{PbTe} = y_{Pb}^I y_{Te}^{II}\,{}^0G_{Pb:Te}^{PbTe} + y_{Pb}^I y_{Va}^{II}\,{}^0G_{Pb:Va}^{PbTe} + y_{Va}^I y_{Te}^{II}\,{}^0G_{Va:Te}^{PbTe} + y_{Va}^I y_{Va}^{II}\,{}^0G_{Va:Va}^{PbTe} + 0.5RT(y_{Pb}^I \ln y_{Pb}^I + y_{Va}^I \ln y_{Va}^I) + 0.5RT(y_{Te}^{II} \ln y_{Te}^{II} + y_{Va}^{II} \ln y_{Va}^{II}) + \Delta G_{mix}^{xs}, \quad (9)$$

where, it is assumed ${}^0G_{Va:Va}^{PbTe} = 0$ due to the unphysical character of having vacancies completely occupy both the sublattices. ${}^0G_{Pb:Te}^{PbTe}$, ${}^0G_{Pb:Va}^{PbTe}$, and ${}^0G_{Va:Te}^{PbTe}$ are given by,

$$\begin{aligned} {}^0G_{Pb:Te}^{PbTe} &= {}^oG_{Pb}^{fcc} + {}^oG_{Te}^{hex} + X_1 + Y_1 \cdot T, \\ {}^0G_{Pb:Va}^{PbTe} &= {}^oG_{Pb}^{fcc} + X_2 + Y_2 \cdot T, \\ {}^0G_{Va:Te}^{PbTe} &= {}^oG_{Te}^{hex} + X_3 + Y_3 \cdot T. \end{aligned} \quad (10)$$

X_i and Y_i are user-defined parameters, that along with ${}^{v}A_{i,j}^{Liq}$ and ${}^{v}B_{i,j}^{Liq}$ in the expansion of the excess Gibbs energy term ΔG_{mix}^{xs} (similar to as in Eq. (6)), are the only unknowns. ${}^{0}G_{Pb:Va}^{PbTe}$ and ${}^{0}G_{Va:Te}^{PbTe}$ are related to the vacancy formation energies on the Te and Pb sublattices, respectively, and the temperature-independent parameters X_2 and X_3 in these expressions are fixed to the vacancy defect formation energies calculated from DFT. The rest of the parameters in Eq. (10) are fitted to experimental data on the phase diagram and thermodynamic data.

2.3.3. Fcc_A1, Hexagonal_A8

The standard reference phases of Pb and Te, fcc and hexagonal, respectively, have been modeled with no solubilities as previous experimental results indicate. Thus, the Gibbs energies of these phases are described by the reference energies ${}^{o}G_{Pb}^{fcc}$ and ${}^{o}G_{Te}^{hex}$.

3. Results and discussion

3.1. Defect stability

The calculated lattice constant of 6.559 Å and formation enthalpy of −0.406 eV/atom of PbTe are in good agreement with the experimental values of 6.462 Å [37], and ≈−0.36 eV/atom [38,39], respectively. However, the calculated direct band gap of 0.82 eV at the L point using GGA over-estimates the value of 0.31 eV obtained from recent experiments [40]. On the other hand, our calculations show that the hybrid HSE functional coupled with SOC leads to an upward shift of the topmost valence band and a downward shift of the lowest conduction band leading to a reduction in the gap to 0.28 eV (for a 0.3 $Å^{-1}$ screening length and 25% Hartree Fock exchange mixing), whereas just including SOC effects results in a gap of 0.08 eV. Both these methods are computationally prohibitive with current supercomputers to be applied to the 250 atom defect supercells used in this work. HSE calculations on smaller supercells would be plausible (but still very expensive), however, the effect of approximations in image-charge and potential alignment correction schemes would then become more pronounced due to the relatively small size of these supercells, thus negating the beneficial effect of using an accurate band gap. This is why a vast majority of defect calculations still employ PBE (or other semi-local or local) functionals coupled with band gap correction schemes, as well documented in the literature [41,42]. Thus, we have just resorted to a well-documented methodology of using GGA for defect calculations together with a band-gap correction scheme that is discussed later in this section.

Three types of point defects are considered in this work on each of the Pb and Te sublattices that make up the PbTe rock salt structure: vacancies (V_{Pb}, V_{Te}), anti-sites (Pb_{Te}, Te_{Pb}), and interstitials (Pb_i, Te_i), all in neutral and charged states ranging from −2 to +2. Formation energies of every defect in each charge state $\Delta H_{d,q}$ are calculated using Eq. (1) taking into account the image charge and potential alignment corrections that are calculated using methods explained in Section 2. Their concave hulls are plotted in Fig. 1 for both Pb-rich and Te-rich growth conditions so as to show only the lowest energy defect as a function of electron chemical potential or Fermi level μ_e. The charge state of the defect corresponds to the slope of these lines. As seen in this figure, the most stable defects with the lowest formation energy for Pb-rich conditions are Pb and Te vacancies (V_{Pb}^{-2}, V_{Te}^{+2}), and for Te-rich conditions are Pb vacancy and Te anti-site defects ($V_{Pb}^{-2}, Te_{Pb}^{+2}$). The most dominant defect is determined by the position of the Fermi level, which in turn is calculated as a function of temperature by solving the charge neutrality condition. Under the assumption of dilute limit of defect concentrations, the number of free charge carriers in the compound is controlled by the number of electrons charged defects can either donate to or accept from the bands. The conservation of charge neutrality condition requires,

$$n - p = \sum_d q_d c_{d,q}, \tag{11}$$

where, n and p are the free carrier concentrations of electrons and holes given by,

$$\begin{aligned} n &= \int_{E_{CBM}}^{+\infty} n(E) f(E;\mu_e,T)\,dE, \\ p &= \int_{-\infty}^{E_{VBM}} n(E)[1 - f(E;\mu_e,T)]\,dE. \end{aligned} \tag{12}$$

$n(E)$ is the density of states of the defect-free crystal, and $f(E;\mu_e,T)$ is the Fermi–Dirac distribution. In the

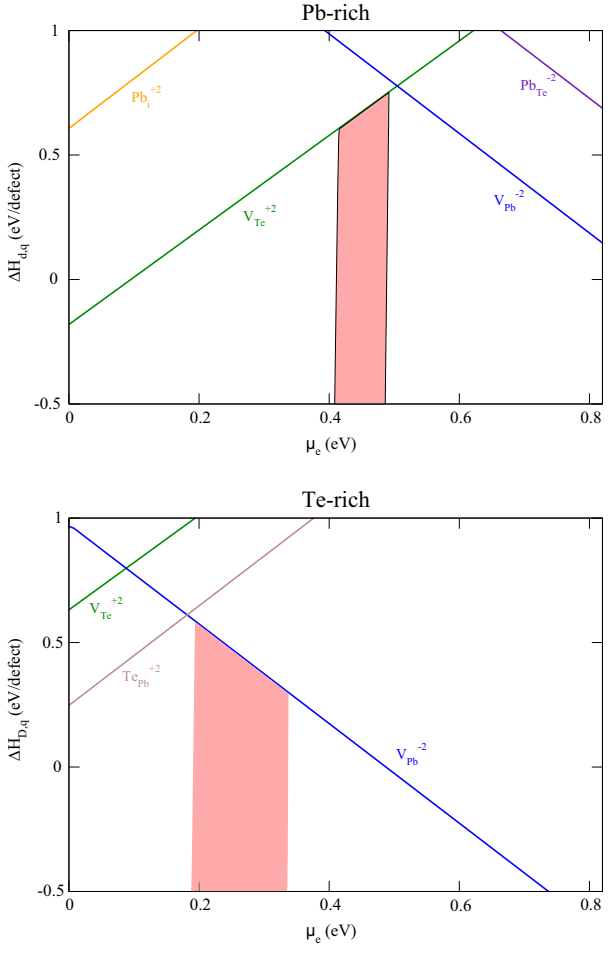

Fig. 1. Calculated defect formation energies, $\Delta H_{d,q}$ in PbTe as a function of Fermi level, μ_e in Pb-rich and Te-rich conditions. Slope of lines corresponds to the charge state of the defect, and shaded areas represent the range of calculated equilibrium Fermi levels shown in Fig. 2.

non-degenerate limit, when Fermi levels are more than several kT below E_{CBM} and above E_{VBM}, the carrier concentrations simplify to [43],

$$n = N_C exp\left(-\frac{E_{CBM} - \mu_e}{kT}\right),$$
$$p = N_V exp\left(-\frac{\mu_e - E_{VBM}}{kT}\right), \quad (13)$$

where, k is the Boltzmann constant, and N_C and N_V are the effective density of states in the conduction and valence bands, respectively, given by,

$$N_C = 2\left(\frac{2\pi m_e kT}{h^2}\right)^{3/2},$$
$$N_V = 2\left(\frac{2\pi m_h kT}{h^2}\right)^{3/2}, \quad (14)$$

where, h is the Planck's constant, and m_e and m_h are the effective masses for the electrons and holes, and are equal to $0.17m_0$ and $0.20m_0$, respectively, for PbTe [43] where m_0 is the mass of an electron. In Eq. (11) above, q_d is the charge of the defect d with concentration $c_{d,q}$. In the dilute limit of defect concentrations, the concentration $c_{d,q}$ of a particular defect in the structure is given by the Botlzmann distribution,

$$c_{d,q} = c_0 e^{-\Delta H_{d,q}/kT}, \quad (15)$$

where, c_0 is the concentration of possible defect sites in the supercell.

Band-gap correction scheme: The GGA functional used in this work results in an erroneous band gap of 0.82 eV because of which we need to correct our defect formation energies. Without doing more computationally expensive hybrid functional or SOC calculations, we have employed a simple projection scheme for this. According to this scheme, the electron chemical potential μ_e is mapped between the carrier concentrations (n and p in Eq. (13)) and defect concentrations ($c_{d,q}$ in Eq. (15)) that assume different band gaps. This mapping is accomplished by turning μ_e into a fractional quantity of the band gaps as,

$$x = \frac{\mu_{e,exp}}{E_{g,exp}} = \frac{\mu_{e,theo}}{E_{g,theo}}, \quad (16)$$

where, $\mu_{e,exp}$ is used in Eq. (13), $E_{g,exp}$ is the temperature dependent experimental band gap from Ref. [40] used in this equation for the calculation of n and p, and $\mu_{e,theo}$ is used in Eqs. (1) and (15) for the calculation of defect energies $\Delta H_{d,q}$ and concentrations $c_{d,q}$ that use the theoretical GGA band gap of $E_{g,theo} = 0.82$ eV. The fractional quantity x can be solved for self-consistently from the charge neutrality condition in Eq. (11) which becomes,

$$N_C exp\left(-\frac{E_{CBM} - \mu_{e,exp}}{kT}\right) - N_V exp\left(-\frac{\mu_{e,exp} - E_{VBM}}{kT}\right) = \sum_d q_d c_0 e^{-\Delta H_{d,q}(\mu_{e,theo})/kT}, \quad (17)$$

where $\Delta H_{d,q}$ is a function of $\mu_{e,theo}$ as in Eq. (1). Solving this equation for x gives us $\mu_{e,exp}$ and $\mu_{e,theo}$ from Eq. (16) above. It is $\mu_{e,theo}$ that is used to represent the electron chemical potential or Fermi level μ_e mentioned in the text of this work, and used in the figures.

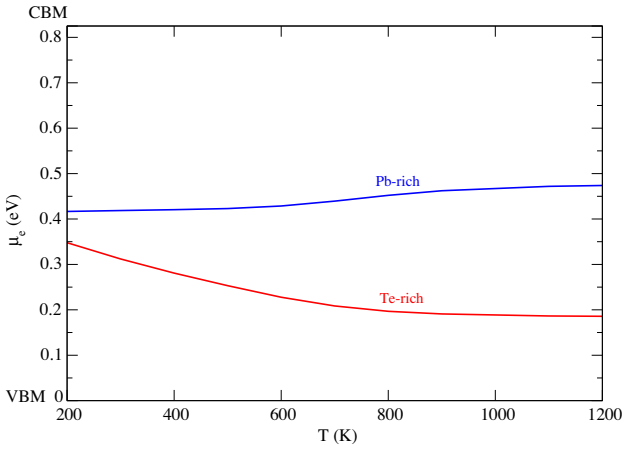

Fig. 2. Equilibrium positions of the Fermi level, μ_e for Pb-rich and Te-rich conditions obtained from solving the charge neutrality equation.

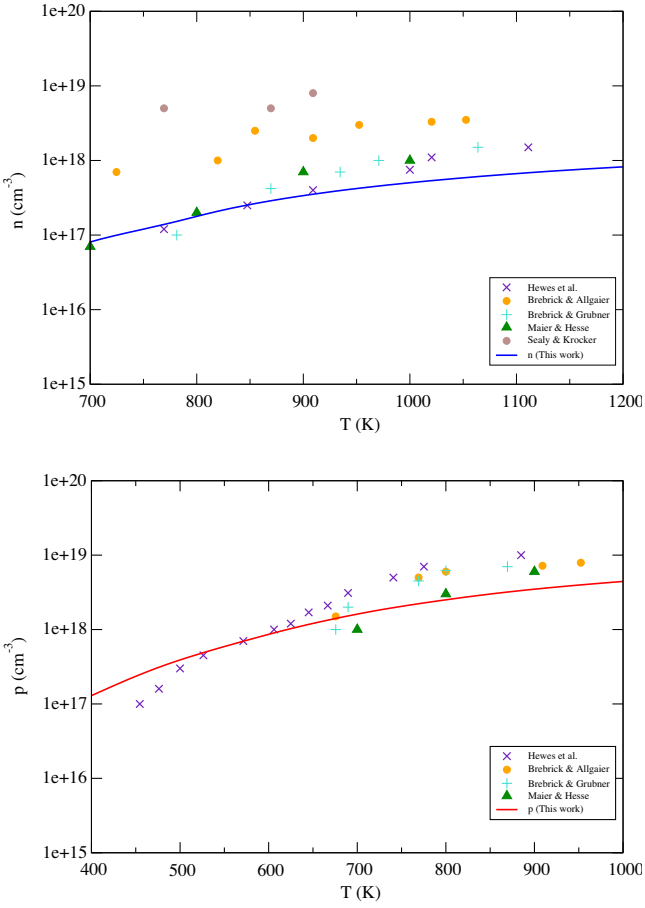

Fig. 3. Calculated concentrations of electrons and holes for Pb-rich and Te-rich growth conditions, respectively, compared with experimental data from Refs. [2–6].

The position of the Fermi level as a function of temperature is determined by numerically solving the charge neutrality condition in Eq. (11) at a range of temperatures, the results of which are shown in Fig. 2 for both Pb-rich and Te-rich growth conditions. This range of Fermi level results in electrons being the dominant carrier for Pb-rich conditions and holes for Te-rich conditions, thus correctly

Table 1. Defect formation energies $\Delta H_{d,q}$ (eV/defect) calculated for each point defect considered in the PbTe system for chemical potentials corresponding to Pb-rich and Te-rich conditions. Values are determined at $\mu_e = 0.42$ eV for Pb-rich and $\mu_e = 0.31$ eV for Te-rich conditions which are the equilibrium Fermi levels (relative to the VBM) obtained at T = 300 K by solving the charge neutrality equation, as shown in Fig. 2. Only the lowest energy charge state for each defect at this Fermi level, corresponding to Fig. 1, is shown.

Pb-rich		Te-rich	
Defect	$\Delta H_{d,q}$ (eV/defect)	Defect	$\Delta H_{d,q}$ (eV/defect)
V_{Te}^{+2}	0.72	V_{Pb}^{-2}	0.35
V_{Pb}^{-2}	0.95	Te_{Pb}^{+2}	0.87
Pb_i^{+2}	1.44	V_{Te}^{+2}	1.32
Pb_{Te}^{-2}	1.49	Pb_i^{+2}	2.04
Te_{Pb}^{+2}	2.71	Te_i^{+2}	2.78
Te_i^{+2}	3.73	Pb_{Te}^{-1}	3.29

predicting *n*-type behavior on the Pb-rich side and *p*-type behavior on the Te-rich side as observed in various experiments [2–8]. The calculated net carrier concentrations are plotted in Fig. 3 which also agree well with these experimental data. The position of Fermi levels leads to vacancies being the most dominant defects for both Pb-rich and Te-rich conditions. Donor defects V_{Te}^{+2} for Pb-rich conditions and acceptor defects V_{Pb}^{-2} for Te-rich conditions are the highest concentration defects that lead to the observed *n*-type and *p*-type behavior, respectively. Table 1 shows the defect formation energies of all defects calculated at the equilibrium value of the Fermi level at 300 K. Experimental evidence of Pb and Te vacancies being the primary point defects in PbTe has been shown through experiments by Brebrick and Grubner [3]. The proposition of Pb interstitials being the dominant defect over Te vacancies for Pb-rich conditions had been suggested earlier by Brebrick and Allgaier [2] due to the instability of Pb-saturated crystals, and Schenk et al. [44] due to the increase of lattice parameter with carrier concentration. However, Brebrick and Grubner [3] later did not see the crystal instability in Pb-rich samples attributing it to impurities, and based on the increasing order of mobility of Te vacancy, Pb vacancy, and Pb interstitial, implied that Pb and Te vacancies were indeed the predominant point defects. Thus, as has been confirmed by the DFT calculations in this work, Pb and Te vacancies are the primary defects in PbTe, and this result along with their formation energies shown in Table 1 has been used in the thermodynamic CALPHAD model of the PbTe phase as discussed in the following section.

3.2. Modification and assessment of the CALPHAD model

The thermodynamic model of the binary Pb-Te system was last calculated and developed by Gierlotka et al. [12] in which the small non-stoichiometry of the PbTe phase was modeled using the Wagner–Schottky defect model [13] for anti-site defects, i.e. $(Pb, Te)_1$:$(Te, Pb)_1$. In a later publication [31], the PbTe phase was assumed to be an ideal defect-free compound. From our DFT calculations in this work, we found that the Fermi level is positioned where vacancy defects have the lowest formation energy, and are thus more stable than the anti-site defects on both the Pb and Te sublattices, i.e. in Pb-rich and Te-rich crystal growth conditions, respectively. Thus, in this work, we have changed the PbTe phase model to consist of vacancies instead – $(Pb, Va)_1$: $(Te, Va)_1$, used the defect formation energies calculated from DFT in its Gibbs energy description, and reassessed the entire Pb-Te thermodynamic model.

The evaluation and optimization of the thermodynamic model was performed using the PARROT module of Thermo-Calc [45] package for the calculation of phase diagrams. The Gibbs free energy G_m^{ϕ} of each phase expected to participate in the equilibrium phase diagram of the system was defined using models as described in Section 2. Parameters X_2 and X_3 in the Gibbs free energy expansion of the PbTe phase shown in Eq. (10) are fixed to the DFT defect formation energies of V_{Te}^{+2} and V_{Pb}^{-2} defects, respectively, shown in Table 1 and as explained earlier in Section 2.3.2. Thus, $X_2 = 0.72$ eV/defect = 69,469 J/mol,

Table 2. Model description and parameters for phases in the Pb-Te system. The functions GHSERPB, GHSERTE, GLIQPB, and GLIQTE are obtained from the SGTE database [32]. Parameters X_2 and X_3 in the Gibbs free energy expansion of the PbTe phase shown in Eq. (10) are fixed to the DFT defect formation energies of V_{Te}^{+2} and V_{Pb}^{-2} defects, respectively, shown in Table 1 and as explained in Section 2.3.2. Thus, $X_2 = 0.72$ eV/defect = 69,469 J/mol, and $X_3 = 0.35$ eV/defect = 33,770 J/mol, as listed below.

Phase	Model	Model parameters (J/mol)
Fcc_A1	Sublattice model $(Pb, Va)_1$	$G_{Pb:Va}^{fcc} = {}^{o}G_{Pb}^{fcc} = \text{GHSERPB}$
Hexagonal_A8	Random solution $(Te)_1$	$G_{Te}^{hex} = {}^{o}G_{Te}^{hex} = \text{GHSERTE}$
Liquid	Associate model $(Pb, Te, PbTe)_1$	$G_{Pb}^{Liq} = \text{GLIQPB}$
		$G_{Te}^{Liq} = \text{GLIQTE}$
		$G_{PbTe}^{Liq} = \text{GLIQPB} + \text{GLIQTE} - 60870.3 + 18.1 \times \text{T}$
		${}^{0}L_{Pb,PbTe}^{Liq} = 20634.8\text{–}9.7 \times \text{T}$
		${}^{1}L_{Pb,PbTe}^{Liq} = 7.9$
		${}^{0}L_{Te,PbTe}^{Liq} = -4167.5 - 2.7 \times \text{T}$
		${}^{1}L_{Te,PbTe}^{Liq} = 3500.9$
PbTe	Sublattice model $(Pb, Va)_1$:$(Te, Va)_1$	$G_{Pb:Te}^{PbTe} = \text{GHSERPB} + \text{GHSERTE} - 128362.3 + 432.9 * \text{T} - 52.9 \times \text{T} \times \text{LN(T)}$
		$G_{Pb:Va}^{PbTe} = \text{GHSERPB} + 69469 + 18 \times \text{T}$
		$G_{Va:Te}^{PbTe} = \text{GHSERTE} + 33770 + 25 \times \text{T}$
		$G_{Va:Va}^{PbTe} = 0$
		${}^{0}L_{Pb,Va:Te}^{PbTe} = 20621.9 - 35.7 \times \text{T}$

and $X_3 = 0.35$ eV/defect = 33770 J/mol, as listed in Table 2. Rest of the parameters entering these models were fitted to available experimental data on the positions of various solubility lines in the phase diagram. The liquidus line was fitted to data determined by DTA and thermal analysis in Refs. [46–50]. The position of the equilibrium lines of the PbTe phase determined through carrier concentration measurements in Refs. [2–4,8,7,5] were used to fit the rest of the user-defined parameters shown in Eq. (10). Experimental measurements of thermodynamic data on this system are also used to optimize parameters of this system. This additional set of experimental data helps impose restrictions to the optimization process by reducing the degrees of freedom, and thus result in a thermodynamically consistent model [51]. The first set of thermodynamic data used is the enthalpy of mixing of the liquid phase that has been measured using the calorimetric method in Refs. [47,52–54]. The second set of thermodynamic data used is the chemical potential of Te in the liquid phase that was determined using partial pressure measurements made in Refs. [55,56] assuming the gaseous phase only contains Te_2.

The set of optimized thermodynamic parameters of the model that form part of the Gibbs free energy functions are listed in Table 2 along with the phase models used. The resulting phase diagram is shown in Fig. 4. The solubility lines of the PbTe phase are shown in Fig. 5 along with solubility lines obtained using defect concentrations calculated using DFT in this work. Both sets of data agree reasonably well with experimental data, and that the solubility on the Pb-rich side is lower than that on the Te-rich side of the stoichiometric line at $x = 0.50$. As is the case with the experimental and CALPHAD-calculated solubility lines, the DFT solubility lines do not meet at the invariant melting point of the phase mainly because the DFT phase boundaries are calculated without considering the liquid phase. If considered, the free energy of which will most likely fall below that of the PbTe phase above its melting point, thus closing the phase boundaries of the PbTe phase at high enough temperatures by making it more stable. But below the melting points, the agreement is fairly good. Figs. 6 and 7 show the resulting thermodynamic data from the CALPHAD model on the enthalpy of mixing of the liquid phase and chemical potential of Te in the liquid phase at 1200 K, respectively, which agree well with experimental literature.

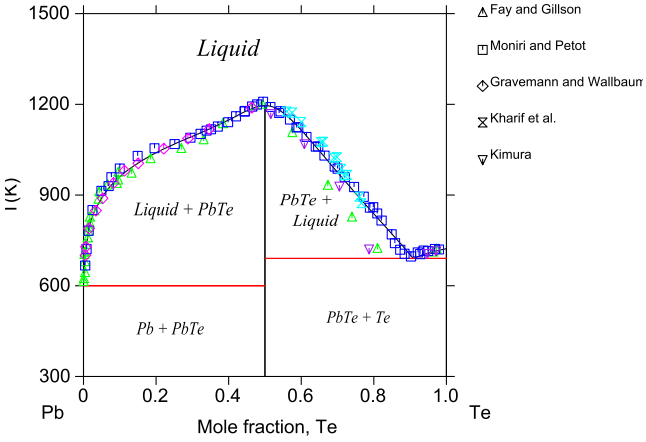

Fig. 4. Pb-Te phase diagram calculated with the CALPHAD method and compared with experimental data.

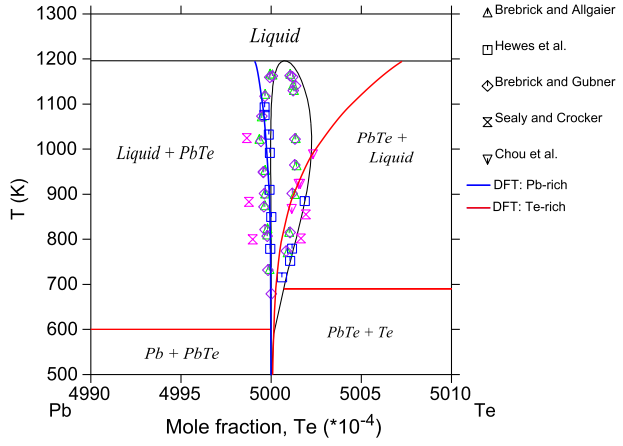

Fig. 5. Solidus lines of the PbTe phase calculated with the CALPHAD method compared with solubility lines calculated from DFT, and with experimental data.

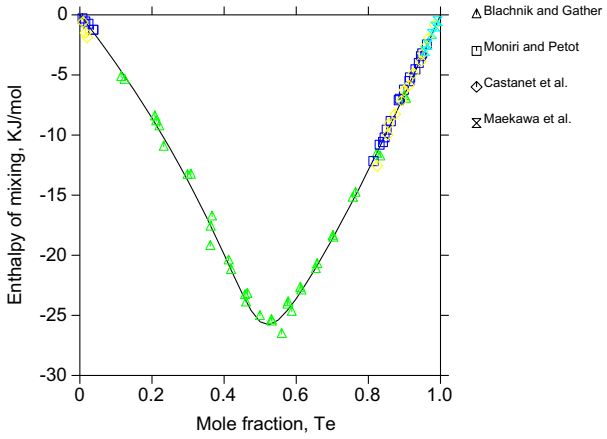

Fig. 6. Enthalpy of mixing of the liquid phase calculated at T = 1200 K with reference to the liquid phase states of Pb and Te, and compared with experimental data.

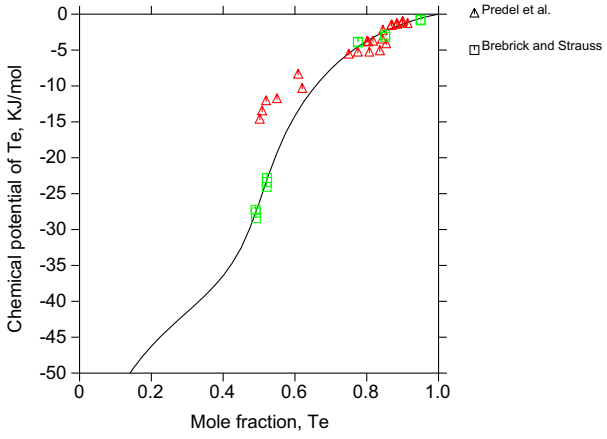

Fig. 7. Chemical potential of Te in the liquid phase calculated at T = 1200 K with reference to the fcc phase of Pb and hexagonal phase of Te, and compared with experimental data.

4. Conclusions and outlook

In this work, first principles calculations of defect energetics are used to understand the thermodynamic stability of different types of point defects in PbTe. For Pb-rich

chemical potentials and crystal growth conditions, we find that the most stable defects with the lowest formation energy are Te vacancies V_{Te}^{+2} and Pb vacancies V_{Pb}^{-2}, whereas those for Te-rich growth conditions are Te anti-sites Te_{Pb}^{+2} and Pb vacancies V_{Pb}^{-2}. The Fermi level is determined at various temperatures by numerically solving the charge neutrality equation, which tells us the equilibrium defect and carrier concentrations for various defects in each charged state for both growth conditions. It is found that the electron donating Te vacancies V_{Te}^{+2} are the highest concentration defects for Pb-rich conditions which are the cause of its *n*-type conductivity. Whereas it is the electron accepting Pb vacancies V_{Pb}^{-2} that are the cause of *p*-type conductivity in PbTe for Te-rich growth conditions. This result, along with calculated electron and hole concentrations agree well with data from previous experimental works.

This information is then used to modify and re-develop the thermodynamic model of the Pb-Te system using the CALPHAD method. Previous thermodynamic model of this system assumed a anti-site defect model for the PbTe phase, i.e. $(Pb, Te)_1$:$(Te, Pb)_1$. However, from our calculations we found that it is actually the vacancy defects that predominate in this phase over anti-site or interstitial defects. Accordingly, the defect model for this phase was changed to $(Pb, Va)_1$:$(Te, Va)_1$. In addition to this, the defect formation energies calculated from DFT were used in the parameters of the Gibbs free energy expression of this phase and the resulting non-stoichiometric range was in very good agreement with experimental data. The entire system was then re-assessed based on experimental information on the phase diagram and thermodynamic data on the mixing enthalpy of the liquid phase and chemical potential of Te in the liquid phase. Thus, in this work, we have demonstrated the use of DFT in conjunction with the CALPHAD method by calculating defect formation energies of various intrinsic point defects in PbTe using DFT, and then using those numbers as input to the thermodynamic model of the technologically important PbTe phase which resulted in solubilities in excellent agreement with experiments. Such a methodology is important for the computation of solubility/stability ranges of dopants in TE materials in different regions of the phase diagrams, that is critical to the fine tuning of TE properties.

Acknowledgements

Support for this work was provided by DARPA-ARO under Grant No. W31P4Q-13-1-0010, the Materials Project which is supported by Department of Energys Basic Energy Sciences program under Grant No. EDCBEE, DOE Contract DE-AC02-05CH11231, and the National Science Council of Taiwan (NSC101-3113-P-008-001). J.W.D and C.W. would like to acknowledge the Revolutionary Materials for Solid State Energy Conversion, and Energy Frontier Research Center funded by the US Department of Energy, Office of Basic Energy Sciences under Award Number DE-SC00010543. The authors acknowledge the Materials and Process Simulation Center (MSC) at Caltech, and the Chemical Engineering Cluster at Texas A&M University for providing computing resources useful in conducting the research reported in this work.

References

[1] G.J. Snyder, E.S. Toberer, Nature Mater. 7 (2008) 105–114.
[2] R.F. Brebrick, R.S. Allgaier, J. Chem. Phys. 32 (1960) 18261831.
[3] R.F. Brebrick, E. Grubner, J. Chem. Phys. 36 (1962) 12831289.
[4] C.R. Hewes, M.S. Adler, S.D. Senturia, J. Appl. Phys. 44 (1973) 13271332.
[5] B.J. Sealy, A.J. Krocker, J. Mater. Sci. 8 (1973) 17371743.
[6] H. Maier, J. Hesse, Org. Cryst. Germanates Semicond. 4 (1980) 145–219.
[7] W.W. Scanlon, Phys. Rev. 126 (1962) 509513.
[8] N. Chou, K. Komarek, E. Miller, Trans. AIME 245 (1969) 15531560.
[9] S. Ahmad, S.D. Mahanti, K. Hoang, M.G. Kanatzidis, Phys. Rev. B 74 (2006) 155205-1–155205-13.
[10] K. Xiong, G. Lee, R.P. Gupta, W. Wang, B.E. Gnade, K. Cho, J. Phys. D: Appl. Phys. 43 (2010) 405403-1–405403-8.
[11] N. Wang, D. West, J. Liu, J. Li, Q. Yan, B.-L. Gu, S.B. Zhang, W. Duan, Phys. Rev. B 89 (2014) 045142-1–045142-6.
[12] W. Gierlotka, J. Lapsa, D. Jendrzejczyk-Handzlik, J. Alloys Compd. 479 (2009) 152–156.
[13] C. Wagner, W. Schottky, Z. Phys. Chem. 11 (1930) 163–171.
[14] N. Saunders, A.P. Miodownik, Pergamon Mater. Ser., 1998.
[15] S.B. Zhang, J.E. Northrup, Phys. Rev. Lett. 67 (1991) 2339–2342.
[16] S. Lany, A. Zunger, Model. Simul. Mater. Sci. 17 (2009) 084002-1–084002-14.
[17] G. Makov, M. Payne, Phys. Rev. B 51 (1995) 4014–4022.
[18] M. Gajdoš, K. Hummer, G. Kresse, J. Furthmüller, F. Bechstedt, Phys. Rev. B 73 (2006) 045112-1–045112-9.
[19] S. Baroni, R. Resta, Phys. Rev. B 33 (1986) 7017–7021.
[20] X. Wu, D. Vanderbilt, D.R. Hamann, Phys. Rev. B 72 (2005) 035105-1–035105-13.
[21] W. Cochran, R.A. Cowley, G. Dolling, M.M. Elcombe, Proc. R. Soc. London A 293 (1966) 433–451.
[22] G. Kresse, J. Hafner, Phys. Rev. B 47 (1993) 558–561.
[23] G. Kresse, J. Hafner, Phys. Rev. B 49 (1994) 14251–14269.
[24] G. Kresse, J. Furthmüller, Comput. Mater. Sci. 6 (1996) 15–50.
[25] G. Kresse, J. Furthmüller, Phys. Rev. B 54 (1996) 11169–11186.
[26] P.E. Blöchl, Phys. Rev. B 50 (1994) 17953–17979.
[27] G. Kresse, D. Joubert, Phys. Rev. B 59 (1999) 1758–1775.
[28] O. Bengone, M. Alouani, P. Blöchl, J. Hugel, Phys. Rev. B 62 (2000) 16392–16401.
[29] J.P. Perdew, K. Burke, M. Ernzerhof, Phys. Rev. Lett. 77 (1996) 3865–3868.
[30] H.J. Monkhorst, J.D. Pack, Phys. Rev. B 13 (1976) 5188–5192.
[31] W. Gierlotka, J. Lapsa, K. Fitzner, J. Phase Equilib. Diffus. 31 (2010) 509–517.
[32] A.T. Dinsdale, CALPHAD 15 (1991) 317–425.
[33] U. Kattner, H.L. Lukas, G. Petzow, CALPHAD 10 (1986) 103116.
[34] J.C. Valiant, T.E. Faber, Philos. Mag. 29 (1974) 571–583.
[35] V.M. Glazov, S.N. Tshizevskaya, N.N. Glozdeva, Liquid Semiconductors, Nauka, Moscow, 1967.
[36] F. Sommer, Z. Metallkd. 73 (1982) 72–86.
[37] K. Koike, T. Honden, I. Makabe, F.P. Yan, M. Yano, J. Cryst. Growth 257 (2003) 212–217.
[38] C. Hirayama, J. Chem. Eng. Data 9 (1964) 6568.
[39] P.M. Robinson, M.B. Bever, Trans. AIME 236 (1966) 814817.
[40] Z.M. Gibbs, H. Kim, H. Wang, R.L. White, F. Drymiotis, M. Kaviany, G.J. Snyder, Appl. Phys. Lett. 103 (2013) 262109-1–262109-5.
[41] C. Freysoldt, B. Grabowski, T. Hickel, J. Neugebauer, G. Kresse, A. Janotti, C. Walle, Rev. Mod. Phys. 86 (2014) 253–305.
[42] S. Lany, A. Zunger, Phys. Rev. B 78 (2008) 235104-1–235104-25.
[43] S.M. Sze, Physics of Semiconductor Devices, second ed., John Wiley & Sons, New York, 1981.
[44] M. Schenk, H. Berger, A. Klimakow, M. Mühlberg, M. Wienecke, Cryst. Res. Technol. 23 (1988) 77–84.
[45] J.-O. Andersson, T. Helander, L. Höglund, P. Shi, B. Sundman, CALPHAD 26 (2002) 273–312.

[46] H. Gravemann, H.-J. Wallbaum, Z. Metallkde 47 (1956) 433441.
[47] M. Moniri, C. Petot, J. Calorim, Anal. Therm. 24b (1978) 195201.
[48] Y.L. Kharif, P.V. Kovtunenko, A.A. Maier, I.K. Avetisov, Russ. J. Phys. Chem. 56 (1982) 1331–1334.
[49] H. Fay, C.B. Gillson, J. Am. Chem. 27 (1902) 8195.
[50] M. Kimura, Mem. Coll. Eng. Kyoto 1 (1915) 149152.
[51] S. Bajaj, A. Landa, P. Söderlind, P. Turchi, R. Arróyave, J. Nucl. Mater. 419 (2011) 177185.
[52] R. Castanet, Y. Claire, M. Laffite, High Temp. High Press. 4 (1972) 343351.
[53] T. Maekawa, T. Yokokawa, K. Niwa, Bussei Kenkyu 17 (1972) 282286.
[54] R. Blachnik, B. Gather, J. Less Common Met. 92 (1983) 207213.
[55] R.F. Brebrick, A.J. Strauss, J. Chem. Phys. 40 (1964) 32303241.
[56] B. Predel, J. Piehl, M.J. Pool, Z. Metallkde 66 (1975) 347352.